

# Superconducting microwave parametric amplifier based on a quasi-fractal slow propagation line

A. A. Adamyan,<sup>1,a)</sup> S. E. de Graaf,<sup>2</sup> S. E. Kubatkin,<sup>1</sup> and A. V. Danilov<sup>1</sup>

<sup>1</sup>*Department of Microtechnology and Nanoscience, MC2, Chalmers University of Technology, SE-41296 Göteborg, Sweden*

<sup>2</sup>*National Physical Laboratory, Hampton Road, Teddington TW11 0LW, United Kingdom*

(Received 28 October 2015; accepted 8 February 2016; published online 22 February 2016)

Quantum limited amplifiers are sought after for a wide range of applications within quantum technologies and sensing. One promising candidate is the travelling wave parametric amplifier which exploits the non-linear kinetic inductance of a superconducting transmission line. This type of microwave amplifier promises to deliver a high gain, a quantum limited noise performance over several GHz bandwidth, and a high dynamic range. However, practical realizations of this type of device have so far been limited by fabrication defects, since the length of the superconducting transmission line required for achieving substantial parametric gain is on the order of  $\sim 1$  m. Here, we report on a design for a microwave traveling wave amplifier based on a slow propagation line comprising a central strip with high kinetic inductance and quasi-fractal line-to-ground capacitors. Due to an enhanced per unit length inductance ( $73 \text{ nH cm}^{-1}$ ) and capacitance ( $15 \text{ pF cm}^{-1}$ ), the line has a microwave propagation velocity as low as  $9.8 \times 10^8 \text{ cm s}^{-1}$ . This translates into parametric gain up to  $0.5 \text{ dB cm}^{-1}$  and a total gain of 6 dB for just a  $\sim 10$  cm long transmission line. Moreover, the flexibility of the presented design allows balancing the line inductance and capacitance in order to keep the characteristic impedance close to  $50 \Omega$  and to suppress standing waves, both factors being essential in order to implement a practical parametric amplifier in the microwave domain.

© 2016 AIP Publishing LLC. [<http://dx.doi.org/10.1063/1.4942362>]

## I. INTRODUCTION

In the fields of circuit quantum electrodynamics<sup>1</sup> and photonics,<sup>2</sup> there has recently been a fast progress in parametric amplifiers to untangle the trade-off between high gain, wide bandwidth, and low noise. Back in the 1950s, it was established that the minimum added noise of a high gain linear amplifier could be equivalent to as low as half-quantum of zero-point fluctuations.<sup>3–5</sup> In contrast, the best semiconductor amplifiers have a thermal noise 40 times higher than the quantum-limit.<sup>6</sup> A similar noise performance is also found in the best (travelling wave-) maser amplifiers.<sup>7</sup> Recent experimental progress in maser amplifiers suggests that these devices may potentially reach quantum limited noise performance,<sup>8</sup> but, inconveniently, masers require high power optical pumping and, typically, strong magnetic field for their operation.

Alternatively, parametric amplifiers have opened up new horizons for realizing the perfect amplifier with noise ultimately limited by quantum fluctuations. Such quantum-limited amplification has recently been achieved in the optical domain with fiber-optical phase-sensitive parametric amplifiers.<sup>9,10</sup> In the optical domain, thermal fluctuations are naturally suppressed, thanks to the single quantum energy being orders of magnitude higher than the environmental temperature. In the microwave domain, thermal fluctuations present a much bigger challenge. Resistive elements contributing to thermal noise need to be excluded

from the amplifier design. Hereof, quantum-limited amplifiers in the microwave domain are to be built solely from superconducting materials.

Parametric amplification relies on a coupling between a pump tone (“pump”) and a signal to be amplified (“signal”) through a non-linearity. The first generation of superconducting parametric amplifiers exploited the non-linear inductance of Josephson junctions.<sup>11</sup> Josephson parametric amplifiers (JPAs) can indeed approach the quantum limit of half a photon of added noise power per unit bandwidth. As the non-linearity inherent to a superconductor is small, to get strong enough amplification in JPAs, the Josephson element is coupled to a resonance cavity. As a result, a signal passing back and forth through the resonance cavity (a segment of superconducting microstrip or coplanar line), coupled to a single non-linear element, acquires a small power gain  $\delta P$  at each passage, so that the total gain becomes  $Q\delta P$  ( $Q$  being the resonator quality factor in the range of 1000 to 10000). Unfortunately, for a resonance amplifier, a  $Q$ -times increased gain is achieved at the expense of  $Q$ -times reduced bandwidth  $\Delta f \sim f_0/Q$  (where  $f_0$  is the cavity resonance frequency), which is usually not more than  $\sim 10$  MHz.<sup>12</sup> In a more recent work, a bandwidth of  $\sim 700$  MHz was obtained, yet with a dynamic range limited by the Josephson energy  $\sim I_c^2/Q$ , where  $I_c$  is the Josephson junction critical current.<sup>13</sup>

To improve the bandwidth, the resonant cavity coupled to a single Josephson junction could be unfolded into a transmission line loaded with periodic array of Josephson elements.<sup>14</sup> In such a Josephson travelling wave parametric amplifier (JTWPA), the signal was instead amplified by

<sup>a)</sup>Electronic mail: [astghik@chalmers.se](mailto:astghik@chalmers.se)

passing through many cascaded junctions. The implementation of this idea resulted in a wide-band amplifier with 6–8 dB average gain and 2–3 dB gain variations, yet for the realization of a practical amplifier, many technical issues remain to be solved. For example, the fabrication of more than 1000 Josephson junctions with near identical parameters is a challenge. (Parameter dispersion will cause reflections in the line and hamper the amplifier operation, as explained further in detail.) Moreover, the dynamic range, as in any Josephson element-based design, is limited by the junction saturation power.<sup>13</sup> And, finally, the most established technique for fabricating Josephson elements relies on aluminum tunnel junctions, which limits the operating temperatures to values well below  $T = 1$  K.

A radically different approach is to exploit the non-linearity linked to the kinetic inductance (KI) of a superconductor, instead of the Josephson junction inductance.<sup>15</sup> Clear advantages of this approach are significantly increased operational temperatures (up to  $T \sim 4$  K) and a higher dynamic range, as compared with Josephson elements. Such Kinetic Inductance Travelling Wave Parametric Amplifiers (KI-TWPA) offer wide-band amplification with an added noise approaching the quantum limit.<sup>16</sup> Another advantage is exploiting the non-linearity intrinsic to the superconducting material, which is more reproducible and controllable as compared with the Josephson junction non-linearity. In practice, for a normal bulk superconductor, the effect of non-linear KI is negligible. High enough KI non-linearity can only be obtained by thin-film technologies producing long and narrow superconducting strips. It is only after a great recent progress in thin film technology and microfabrication that KI-TWPAs have become an approachable task and have proved to be promising candidates for the implementation of a practical parametric amplifier.<sup>17</sup>

For the proof-of-concept superconducting KI-TWPA reported in Ref. 17 to have sufficient KI non-linearity for achieving  $\sim 10$  dB average gain, a  $\sim 1$  m long,  $\sim 1$   $\mu$ m wide, and 35 nm thick NbTiN line was used as the central coplanar waveguide (CPW) line of KI-TWPA. Such a long, narrow, and thin strip has resulted in two major problems: weak spots on the line, limiting the maximum obtainable pump power, and a high characteristic impedance of the transmission line, causing strong reflections on the terminals and therefore frequency dependent gain. In the quest for a practical parametric amplifier, these issues constitute significant drawbacks. In what follows, we shall discuss these issues in more detail.

In terms of fabrication, even with the best fabrication facilities, it is hardly realistic to expect a line with 35 nm thickness and 1:1 000 000 aspect ratio to be free from fabrication imperfections and defects; the longer is the line the more likely it will have a weak spot. For example, it was demonstrated by Bockstiegel *et al.*,<sup>18</sup> that a 2 m long line does not provide a gain higher than a 1 m long line for this very reason.

To achieve the desired non-linearity, a thin and narrow strip with high KI is needed. The characteristic impedance of such a line is much higher than the typical microwave input/output circuitry impedance of  $50 \Omega$  ( $\sim 300 \Omega$  for a design reported in Ref. 17). Such a strong impedance mismatch is a

serious issue: reflections at the ends of the amplifier line create standing waves, in analogue to a Fabry-Pérot cavity.<sup>19</sup> These standing waves cause ripples in the transmission spectra, thus making the device gain frequency-dependent (fluctuating by more than  $\sim 10$  dB), which is not acceptable in most applications. Eliminating impedance mismatch-caused reflections is very challenging and previous attempts to achieve impedance matching by deploying adiabatic tapers as impedance transformers were not yet completely successful.<sup>17,18,20,21</sup> While the standing waves do not contribute to the gain (since only the traveling wave propagating synchronously with the signal matters for the gain), they are responsible for the premature break down of superconductivity, which limits the maximum achievable gain.

In this work, we report on a KI-TWPA based on a slow propagation line, where the high KI of the central line is balanced with quasi-fractal, inter-digitated capacitors. Such design naturally addresses both problems mentioned above: First, by balancing the high KI of the line with increased capacitance, we successfully shift the transmission line impedance down, ultimately to  $\sim 50 \Omega$ . Second, by reducing the propagation velocity, we make the line physically shorter for a given electrical length. Such a considerably short and robust central line translates into a uniform linewidth with less number of fabrication defects, bringing us closer to a practical quantum-limited amplifier.

## II. DESIGN AND OPERATION PRINCIPLE

### A. TWPA operation

The KI-TWPA exploits the non-linearity of kinetic inductance, fundamentally inherent to any superconducting material<sup>15</sup>

$$L_K(I) \approx L_K(0)(1 + (I/I_*)^2), \quad (1)$$

where  $I$  is the current,  $L_K(0)$  is the geometrical inductance, and  $I_*$  is the non-linearity parameter. This non-linearity mixes propagating waves in the transmission line through the concept of four way mixing:<sup>17</sup> the strong pump ( $\omega_p$ ), the idler ( $\omega_i$ ), and the weak input signal ( $\omega_s$ ) subject to amplification, as a result of which two pump photons are converted into one photon in the idler mode and one in the signal mode  $2\omega_p = \omega_i + \omega_s$ , thus amplifying the weak input signal. The maximum achievable parametric gain is linked to the non-linearity of the transmission line

$$G \approx \exp(\Delta\theta)/4, \quad (2)$$

where

$$\Delta\theta = (\theta/2)(I/I_*)^2 \quad (3)$$

is an additional phase shift acquired by a microwave signal in response to a current  $I$  through the transmission line due to the non-linearity. The non-linear phase shift  $\Delta\theta$  is proportional to the electrical length (total input-output phase shift acquired by a small signal)

$$\theta = 2\pi L_{10}f/v_f, \quad (4)$$

where  $L_{\text{tot}}$  is the total physical length of the line,  $f$  is the microwave frequency, and  $v_f$  is the phase velocity. According to Bardeen-Cooper-Schrieffer (BCS) theory, the maximum non-linearity is limited by the constraint  $I_* > I_c/0.52$ , where  $I_c$  is the line critical current.<sup>22</sup> For design parameters as in Ref. 17, according to Eqs. (2) and (3), an electrical length of  $\theta \sim 500\text{--}1000$  rad and a line  $\sim 1$  m long are required to achieve 10 dB average gain. Such CPW parameters make the line vulnerable to fabrication defects and difficult to interface the line high impedance to the  $50\ \Omega$  circuitry.<sup>17</sup>

Another design goal to be considered when implementing a KI-TWPA is dispersion engineering. To achieve maximum gain, the signal and the pump should be properly synchronized all the way through the transmission line.<sup>1</sup> However, a non-linearity of line KI implies that the weak signal and the strong pump will have different phase velocities and therefore lose synchronization when propagating across the line. To keep the signal and the pump synchronized, dispersion engineering is needed, so that the frequency- (dispersive) and amplitude-dependent (non-linear) corrections to the phase velocity will conceal each other. To this end, both in Ref. 17 and in follow-up experiments,<sup>18,20</sup> the transmission line was loaded with periodic perturbations of the central strip width. In the present design, we exploit a similar approach.

## B. KI-TWPA design

Our design for a KI-TWPA based on a slow propagation line is presented in Fig. 1. The main idea is to balance the high KI of the line with an increased per-length capacitance shown in Fig. 1. The basic design element is a 4th-order quasi-fractal pattern,  $52\ \mu\text{m}$  long, depicted in Fig. 1(a). For clarity, one plate of the fractal capacitor coupled to the high KI central line is colored in red, while the other

plate (the fractalized ground plane) is shown in blue. The same area is illustrated in SEM image in Fig. 1(b). In such a fractal design, microwave currents are split into many secondary, tertiary, etc., branches, all connected in parallel. Due to these many parallel connections, the equivalent internal inductance of the fractal unit is much lower than for a simple first-order interdigitated capacitor with the same perimeter. This allows us to maximize the capacitance while minimizing the inductance of the capacitive element.<sup>23</sup> On the next design level, a group of 30 basic fractal units form a single arc section (Fig. 1(e)), and 73 repetitions of the same arc section compose the whole amplifier line (Fig. 1(f)). To fit the design onto a 2 in. wafer, the amplifier line is shaped as a meander, where four four-retour sections (for example, sections 1 and 2 in Fig. 1(f)) were implemented as alternating left/right turning arcs, while U-turns (like sections 2 and 3 in Fig. 1(f)) as one way turning segments. The rationale behind this design is to ensure that the line characteristic impedance is exactly the same for straight and U-turn sections, in order to avoid reflections in the line. The total physical length of the presented line is only 114 mm, i.e., about seven times shorter than the original design reported by Eom *et al.*<sup>17</sup> As the line impedance is close to  $50\ \Omega$ , no impedance conversion to terminals is needed, and to couple  $w \sim 1\ \mu\text{m}$  center line to  $200\ \mu\text{m}$  bonding pads we use simple straight tapers (Fig. 1(f)).

We present two design versions shown in Figs. 1(c) and 1(d). In the first design (Fig. 1(c)), the whole structure is defined in a single, high-KI NbN layer. However, it is in many ways advantageous to restrict the high-KI area to a central strip only, where the KI is actually needed. To this end, we have established a fabrication technology, where the whole design structure is first defined in a thick, low-KI NbN-Al-Nb-NbN multilayer; the need-to-be highly inductive

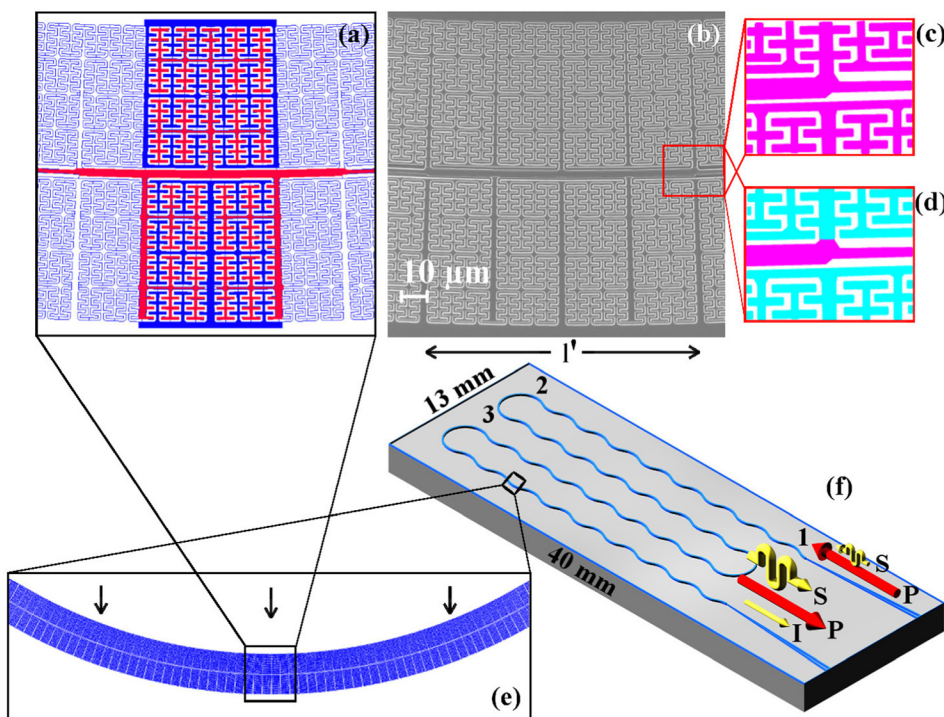


FIG. 1. (a) Design sketch of a basic KI-TWPA fractal unit, one plate of the fractal capacitor coupled to high-KI central line is colored in red, the other plate (the fractalized ground plane) is colored in blue. (b) SEM image of a KI-TWPA unit fractal. (c) and (d) Zoom-in on the SEM image presenting two design versions: all design elements defined in high-KI film (colored in magenta), and a combined design exploiting both high and low-KI (colored in cyan) elements. (e) An arc section with arrows pointing at dispersion engineering element positions. (f) Sketch of the KI-TWPA amplifier chip with dimensions  $13 \times 40$  mm, red/yellow arrows picture the incident pump/input signals and output pump/idler/amplified input signals.

central strip later on is thinned down to a base NbN layer to increase the kinetic inductance. The resulting design is presented in Fig. 1(d). For the multilayer structure, it becomes a much easier task to simulate and obtain a predictable behavior of all fractal elements and interface tapers. Most importantly, implementing fractal structures and the ground plane as low inductive elements allows to shift the frequencies of most unwanted spurious resonances above the operation range of the amplifier (see Section IV for a detailed discussion).

To achieve phase matching, we arrange dispersion engineering by periodic insertions of central strip sections with an increased width, which locally perturb the line impedance. Such periodic perturbations result in stop bands in the transmission spectrum,<sup>24</sup> and close to the rejection gaps the phase velocity  $v_f$  is strongly perturbed. The arrows in Fig. 1(e) point to the locations of dispersion engineering elements: each unit arc contains three equally spaced local perturbations with lengths  $l \sim 78 \mu\text{m}$ ,  $l' \sim 104 \mu\text{m}$ , and  $l'' \sim 208 \mu\text{m}$ , so that the whole  $l - l' - l''$  pattern is repeated with a period corresponding to an arc length  $l_{\text{arc}} = 1560 \mu\text{m}$ . Thus, the  $l - l' - l''$  pattern period defines the microwave wavelength  $\lambda = 2l_{\text{arc}}$ , corresponding to the first rejection gap at a frequency  $f_1 = v_f/\lambda$ , while the element-to-element distance  $l_{\text{arc}}/3$  defines two extra band gaps at frequencies  $2f_1$  and  $3f_1$ . The highest frequency stop-band at  $3f_1$  is needed to suppress shock wave formation of the pump.<sup>25</sup> The lengths of dispersion elements  $l, l', l''$  define how deep and wide the rejection bands are, and so they are fine tuned to maximize the dispersive effect on the phase velocity for frequencies approaching, but still outside the stop bands. To compensate for the non-linear phase shift, one can then tune the pump tone frequency close to a band gap at  $f_1$  or  $2f_1$ .

### III. DEVICE FABRICATION

The main fabrication steps are described in detail in our recent work on a multilayer technology that enables the implementation of high/low KI elements in the same microwave circuit.<sup>26</sup> Here, we will outline the fabrication details specific to the implementation of KI-TWPA for both all-high-KI (Fig. 1(c)) and combined high/low-KI (Fig. 1(d)) designs.

We started the fabrication of all-high-KI sample by sputtering a single 140 nm NbN film on a 2 in., intrinsic Si wafer, while for the combined high-low KI sample, we sputtered a multilayer consisting of NbN (80 nm), Al (20 nm), Nb (100 nm), and NbN (10 nm). Intrinsic Si wafers were dipped in 2% HF bath for 30 s to remove native oxide prior to thin film deposition. To achieve a uniform film thickness over the whole wafer (and therefore the same KI and line impedance), the sputtering was done with a rotating sample stage.

Since the fractal pattern perimeter is  $\sim 6.4 \text{ m}$ , the fabrication of such a long and narrow gap ( $\sim 1 \mu\text{m}$ ) is rather challenging, as a single short will render the whole device useless. Such a short can be caused by any dust particle larger than  $1 \mu\text{m}$ , which would mask some metal to be etched. Dust particles can end-up on the sample during sputtering (flakes from the target), resist spinning, or etching (etch residues). Note that MC2 Nanofabrication Laboratory

has Class 100–300 (ISO 5), equivalent to maximum  $100\,000 \text{ particles m}^{-3}$ .

An increased perimeter and therefore higher vulnerability to shorts is inherent to the fractal design. With a fractal design, we trade the chance of having a weak spot in the shorter central line for an increased probability of line-to-ground short. There is, however, a crucial distinction between these two types of defects which makes this trade-off justified. Any defect, which even partially reduces the central line width, results in a weak spot. In contrast, to get a short, the defect should squeeze the gap completely, which is less likely. Moreover, the weak spots are irreparable, while the shorts can be fixed with ion milling, provided that there are not too many of them.

To minimize the number of shorts, the design was patterned with electron beam (e-beam) lithography and etched all the way through to the substrate twice, using alignment marks to match two exposures (all-high-KI sample was etched twice with  $\text{NF}_3$  gas, while combined high/low KI sample was etched first with  $\text{NF}_3$ , then with  $\text{CF}_4/\text{O}_2$  mixture to avoid attacking bottom NbN in the multilayer, see Ref. 26). This double exposure/etch technique ensured that the un-etched metal after the first exposure/etch step got etched for sure in the second round. Additionally, to avoid shorts due to stitching errors, at each round, the pattern was exposed with two different field boundaries (each with half a base dose). For the combined high/low-KI design, the central line was exposed a third time to selectively thin it down by etching away top NbN/Nb and removing Al in a wet etch solution. The resulting high-KI central line has a single (80 nm) layer of NbN, colored in magenta in Fig. 1(d). The rest of the device, i.e., low-KI elements (fractal capacitor, ground plane, and tapers colored in cyan in Fig. 1(d)) remains as 80/20/100/10 nm multilayer structure of NbN/Al/Nb/NbN.

After all measures taken to reduce the number of shorts, we still got 2–3 shorts per device as shown in Fig. 2(a).

These remaining imperfections were eliminated by focused ion beam (FIB)-SEM milling. The FIB-SEM system was equipped with tilted ion beam column to enable direct SEM viewing of the area being FIB-milled (Fig. 2(b)).

As the shorts present a serious fabrication problem, it was preferential to use a sapphire substrate, where the shorts can be detected with a simple multi-meter test at room temperature. In contrast, for intrinsic Si substrate, shorts were only detectable after cooling down the sample due to the conductivity of Si at room temperature. Unfortunately, the

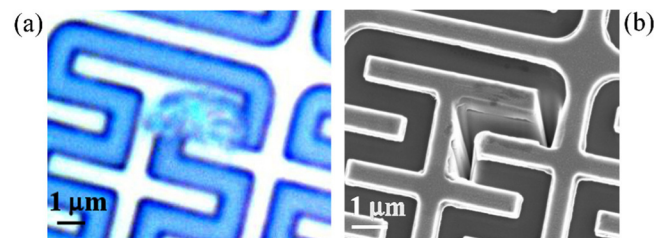


FIG. 2. (a) SEM image of a fractal area with a dust particle acting as a short. (b) SEM image of the fractal area after FIB-SEM milling of the dust particle.

etching result for sapphire on a wafer-scale was not as controllable and uniform as in the case of Si. Hence, to avoid the deterioration of the central line non-linear properties due to non-uniform thin down all over the wafer, samples presented in this work were fabricated on 2 in. intrinsic Si wafers.

## IV. MEASUREMENTS

### A. Line transmission and parametric gain

Devices were characterized in a Helium gas-flow cryostat with a base temperature of 1.8 K. Device input-output terminals were bonded to sampling lines on a printed circuit board (PCB) and microwave transmission (S21) was measured with a vector network analyzer (VNA). To double-check that none of the spikes on the transmission is due to residual reflections on PCB input-output connectors, the S21 was re-measured with two surface-mount 6 dB attenuators mounted close to connectors. Also to eliminate spurious ground plane resonances, many aluminum bonds were made across the KI-TWPA line all over the chip (Fig. 3(a)) and chip ground plane was carefully bonded to PCB ground all around the chip perimeter.

The S21 transmission measured on the all-high-KI device (design in Fig. 1(c)) defined in a uniform 140 nm NbN film is presented in Figs. 3(b) and 3(c), top, in blue. As seen in the transmission spectrum (Fig. 3(c), top), our first attempt to shift line impedance down to  $50 \Omega$  by balancing the high-KI of the central line with high-KI fractal capacitors was not fully successful: some residual ripples are still present on the transmission plot. This, however, is not an unexpected result, since it is very challenging to predict the exact value for the kinetic inductance in advance. Still, the residual ripple amplitude is only  $\sim 1.5$  dB (see Fig. 3(b)), which corresponds to a moderate impedance mismatch between  $50 \Omega$  sampling lines and a line impedance of  $\sim 70 \Omega$  (consistent with the simplified model simulated in Microwave Office).

From the data presented in Fig. 3, we can estimate the basic transmission line parameters. The ripple period of  $f_r = 43$  MHz corresponds to signal propagation time of 11.6 ns (consistent with time domain reflectometry measurements, see below). Given the total line length of  $L_{\text{tot}} = 114$  mm, we arrive at a phase velocity of only  $v_f = 2L_{\text{tot}}f_r = 0.033c$ , compared with that of  $0.1c$  in the original work,<sup>17</sup> where  $c$  is the speed of light in vacuum. The line impedance  $Z = \sqrt{L/C} \approx 70 \Omega$  and the phase velocity  $v_f = 1/\sqrt{LC} \approx 0.033c$  translate into  $L = 7.3$  nH  $\text{mm}^{-1}$  and  $C = 1.5$  pF  $\text{mm}^{-1}$  per-unit-length inductance and capacitance of the line, and for a basic fractal unit with a length of  $52 \mu\text{m}$  we arrive at  $L_{\text{uf}} = 0.38$  nH and  $C_{\text{uf}} = 78$  fF.

The data in Fig. 3 demonstrate that we successfully achieved both primary design targets: substantially reduced line impedance and phase velocity. The former resulted in reduced ripple amplitude and the latter is beneficial for having a shorter and a less defect-prone KI-TWPA line. However, we see that strong ripples in the transmitted signal are still present at frequencies above  $\sim 4$  GHz. One cause for this could be that at high enough frequencies the effects due to discrete nature of fractal line come into play. To understand if this could be the case, we first estimate a characteristic self-resonance frequency of a single fractal unit:  $\omega_{SR} \sim 1/\sqrt{L_{\text{uf}}C_{\text{uf}}} = 2\pi \cdot 29$  GHz. By design, the inductance of the primary branch of the fractal element (cf. Fig. 1(a)) should be on the same page as  $L_{\text{uf}}$ ; we therefore conclude that all self-resonances of a fractal unit are well above the relevant frequency range. At frequencies below  $\omega_{SR}$ , the line can be treated as a lumped element  $(L_{\text{uf}}/2) - (C_{\text{uf}}/2) - (L_{\text{uf}}/2) - \dots$  ladder with a cutoff frequency  $\omega_c \sim 4/\sqrt{L_{\text{uf}}C_{\text{uf}}} = 4\omega_{SR}$ . Even at 10 GHz frequency, the characteristic impedance of such a ladder differs from  $\sqrt{L/C}$  by a factor of  $\sqrt{1 - (2\pi \cdot 10 \text{ GHz})^2 / (4\omega_{SR})^2} \approx 0.996$ , i.e., by 0.4% only. With all discretization effects being of so minor importance, the design can be effectively considered as a continuous coplanar line.

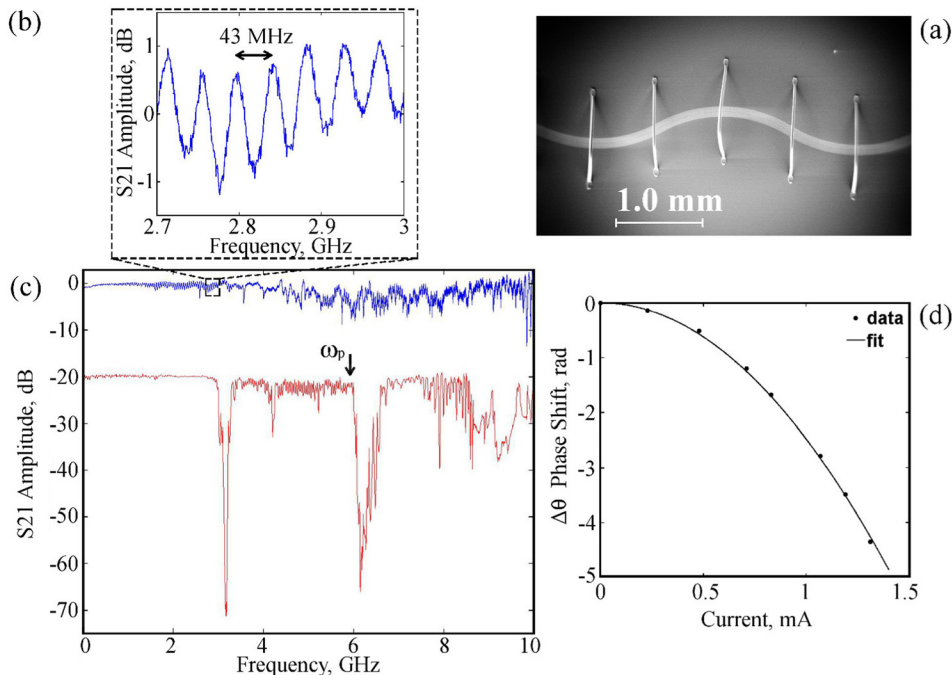


FIG. 3. (a) SEM image of 3 arc sections of KI-TWPA line with wire bonds on top. (b) Zoom in on S21 transmission spectrum of all-high-KI line. (c) Transmission spectra of all-high-KI, single NbN layer device (top, in blue), and combined high/low-KI device (bottom, in red). The measurements were performed at 2.3 K with microwave signal power  $-55$  dBm and zero d.c. through the central line. Background attenuation in input-output lines is subtracted from the transmission data; the bottom (red) plot is offset for clarity. (d) The non-linear phase shift of the combined high/low-KI device in response to a d.c. passed through the center strip. Points: phase shift measured at 5.9 GHz, line: quadratic fit to experimental data corresponding to  $I^* = 9.3$  mA.

A crucial observation is that the high frequency ripples have no specific period, and the exact ripple pattern depends on the arrangement of the bonding wires across the line. An extensive bonding helps to reduce the problem, though does not eliminate it completely. We can therefore attribute these stochastic features to the line being coupled to spurious ground plane resonances which are commonly present at frequencies above a few GHz. Though the exact spectrum of spurious resonances can hardly be predicted, we note that for our design three factors unfavorably shift the spectrum to the low frequency range: the relatively big chip size, the meander-shaped ground plane, and the high KI of the ground plane. While the first two factors are immanent to the presented design, the last one can be eliminated by implementing all design elements except the central strip as low KI structures.

Indeed, the S21 transmission measured on a similar design defined with a multilayer technology (see Fig. 1(d)) is obviously cleaner up to  $\sim 8$  GHz, see Fig. 3(c). For the design presented in Fig. 1(d), the line was loaded with periodic perturbations of the central strip width to achieve dispersion engineering. The basic period of the dispersion engineering pattern is the same as the arc length  $l_{\text{arc}} = 1560 \mu\text{m}$ , which corresponds to the first dispersion band frequency  $f_1 = v_f / 2l_{\text{arc}} = 3.17$  GHz, in agreement with well-defined  $f_1$  and  $2f_1$  stop bands in Fig. 3(c). However, the  $3f_1$  stop band, which is expected to be at  $\sim 9.5$  GHz, is not so well defined. This noticeably correlates with stochastic ripples in the transmission spectrum developing at high frequencies and corroboratively supports our claim that all deviations from an idealized theoretical model are due to the coupling to spurious ground plane resonances. Indeed, the stop band formation is a cumulative effect of coherent reflections on many dispersion elements and is very sensitive to any aperiodic perturbations of the line structure. Also, coupling to spurious resonances effectively opens bypath channels for microwave propagation, thus making transmission non zero even within the stop band.

To characterize the non-linear properties of the transmission line, which are crucial for achieving the parametric gain, we measured the electrical length (the total input to output phase shift) dependence on the d.c. bias. The data in Fig. 3(d) show that the maximum achievable non-linear phase shift is  $\Delta\theta \sim 4.5$  rad. For the total electrical length of  $\sim 427$  rad (from Eq. (4)), this translates into maximum non-linearity of  $\Delta\theta/\theta \sim 1\%$ , which is higher than the 0.7% previously reported in the literature.<sup>17</sup> Fitting the phase response curve to parabola, we extract the non-linearity parameter  $I_* = 9.3$  mA, which is not far from the theoretical limit: BSC theory predicts that the current-induced effect on kinetic inductance could be maximum  $L_K(I_C)/L_K(0) = 1.27$ ,<sup>22</sup> which corresponds to the constraint  $I_* > 1.9I_C = 2.5$  mA. Finally, the measured d.c. critical current is  $I_C = 1.3$  mA (Fig. 3(d)), which for a central line cross section of  $80 \times 800 \text{ nm}^2$  corresponds to a current density  $i_c = 2 \text{ MA cm}^{-2}$ , comparable with the best numbers in the literature,<sup>27,28</sup> which also highlights the high-quality and uniformity of the presented line.

The device operation as a parametric amplifier is presented in Fig. 4. Same as in the original paper by Eom *et al.*,<sup>17</sup>

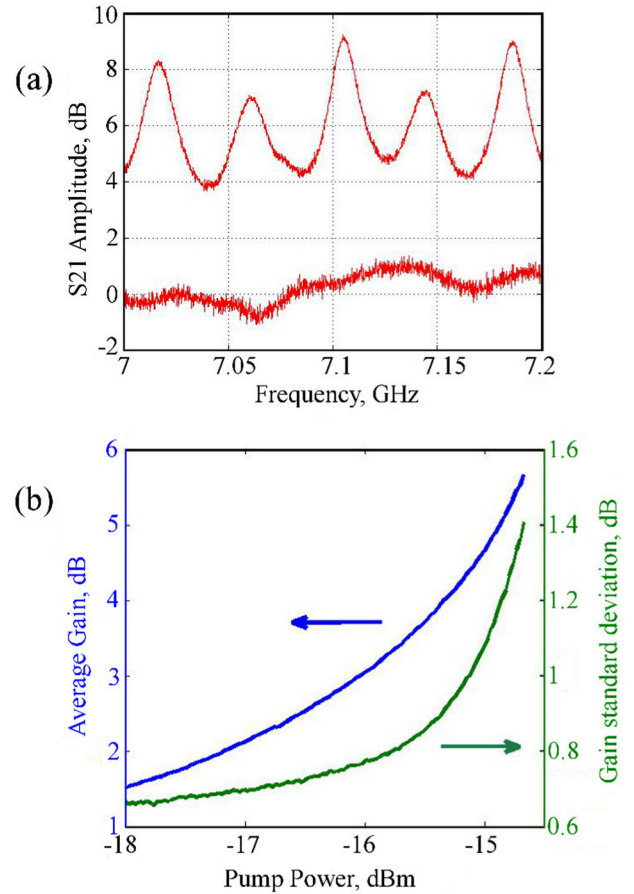


FIG. 4. (a) Measured transmission signal with the pump tone off (bottom), and the pump tone set to maximum ( $-14.7$  dBm, top), showing an average gain of 6 dB. (b) The measured average gain as a function of pump power (in blue, left y axis), ripple amplitude (standard deviation from the average gain) as a function of pump power (in green, right y axis).

we found the dispersion phase shift at the first band gap to be too weak to compensate for the non-linear phase shift at a strong pumping power, and therefore we chose to operate the device with a pump tone around the left side of the second band at  $\sim 6$  GHz (shown with an arrow in Fig. 3(c)). Fig. 4(a) represents the line transmission without pump tone (bottom curve) and for a pump tone set to maximum (i.e., just below the breakdown of superconductivity). Fig. 4(b) (blue plot) represents an average gain as a function of the pump power. We see that although the line is only 114 mm long, the maximum gain is  $\sim 6$  dB. As expected, due to the substantially reduced propagation velocity, the  $\sim 0.5 \text{ dB cm}^{-1}$  per-unit-length gain for our design greatly exceeds the corresponding number for CPW-based parametric amplifiers ( $\sim 0.1 \text{ dB cm}^{-1}$  as reported in Ref. 17). Unexpectedly, we found that when the pump tone power approaches the maximum, some minor ripples start to develop on the transmission plot. As can be seen in Fig. 4(b), the ripples appear only 1 dB below the breakdown of superconductivity which happens at  $-14.7$  dBm pump power. This could be an indication that the line goes into an extremely non-linear regime, where a simplified model for gain in Eq. (2) might not apply. In addition, we could not exclude that these ripples are due to signal reflection on the weak spots in the line, where superconductivity is almost suppressed (see Section IV B for more data on the weak spot formation).

## B. Line homogeneity and maximum pump power

To check the line homogeneity and to understand how the breakdown of superconductivity happens, we performed Time Domain Reflectometry (TDR) measurements, presented in Fig. 5.

Two small dips (b1 and b2) on the TDR plots are due to partial reflection on the input/output bonding wires, so we see that the line propagation time  $t_{i0} \approx 12$  ns (tapers included) matches the ripple period  $f_0 = 43$  MHz on the transmission (cf. Fig. 3(b)). Note that the time axis on TDR plot represents the total four-retour excursion time, which is twice longer than one way propagation time. The fast ripples with a period  $l_{\text{arc}}/v_f = 2 \times 0.16$  ns (inset in Fig. 5(a)) are due to reflections on the dispersion engineering structures. The slow

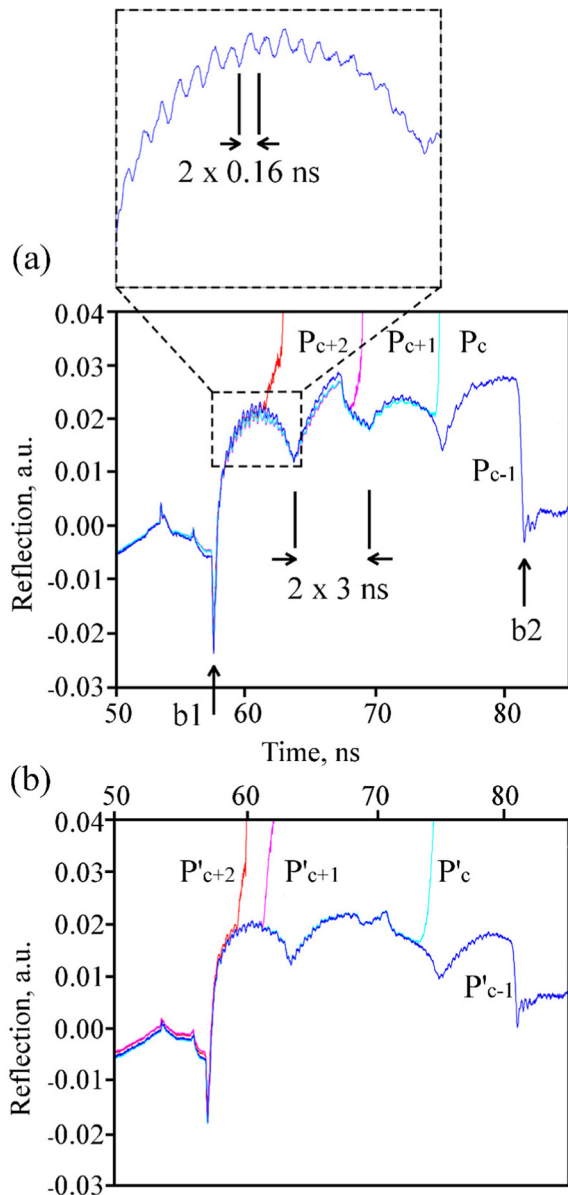


FIG. 5. (a) TDR plot showing superconducting to normal state transition of the line due to increasing pulse power: 1 dB below critical power ( $P_{c-1}$ ), critical power ( $P_c$ ), 1 dB and 2 above critical power ( $P_{c+1}$  and  $P_{c+2}$ ). (Inset) zoom-in on reflection ripples. (b) Similar plot measured with line in-out direction opposite to that in (a), showing different positions of superconductivity breakdown points.

impedance modulation with a period  $\sim 2 \times 3$  ns corresponds to four turns in the meander structure. From these data, we can see that for our fractal line the arc curvature noticeably affects the line impedance. This is because of the relatively high transversal dimension  $d_t = 117 \mu\text{m}$  of the fractal structure: given the arc radius  $R_{\text{arc}} = 1500 \mu\text{m}$ , we arrive at the relative curvature  $d_t/R_{\text{arc}} \approx 1:13$  which is indeed much higher than for a typical CPW line design. It is the high relative curvature which calls for the alternating left/right turning arc design for straight sections of meander structure (cf. Fig. 1). The TDR plots taken at increased pulse voltages clearly show that at critical amplitude the superconductivity in the line first breaks at some weakest point  $P_c$  (see Fig. 5(a), in cyan), when the excitation power is increased by  $\sim 1$  dB the line fails at some point  $P_{c+1}$  closer to the input, at still higher power at point  $P_{c+2}$ , etc. The TDR plots taken for the opposite direction of the excitation pulse reveal a complementary hierarchy of the weakest—second-weakest—etc. points. Importantly, the highest and the lowest excitation powers in the hierarchy differ by approximately 3 dB. This implies that the line is quite close to being homogeneous, and yet a perfectly homogeneous line should withstand a 3 dB higher power and deliver a maximum gain  $\sim 10$  dB (through extrapolation of Fig. 4(b)) or above  $\sim 1 \text{ dB cm}^{-1}$ . On the other hand, the observed pattern of weak spots suggests that in a two times longer line there will likely be a spot with 1 dB lower critical power, so that the maximum gain will be 9 dB, and not  $2 \times 6 = 12$  dB as one would expect for two amplifiers coupled in series.

The picture of the weak spot hierarchy is further supported by the dependence of the superconductivity breakdown power on the pump frequency, presented in Fig. 6. Noticeably, the maximum power varies by  $\sim 2$  dB, on par with the critical power dispersion in the hierarchy extracted from TDR measurements. Also, the dependence is quasi-periodic with a characteristic period close to the 43 MHz period of Fabry-Pérot resonances.

The most straightforward interpretation for the data in Fig. 6 is as follows: the partial reflection of the pump tone

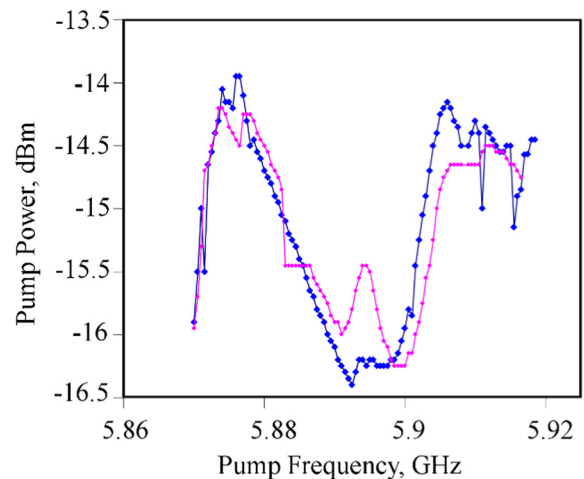


FIG. 6. The maximum pump tone power the line can withstand without breaking superconductivity before (magenta) and after (blue) the sample was extensively bonded.

leads to standing waves formation in the line; when the pump tone frequency is swept the standing wave pattern changes, and so is the local amplitude at the weakest spot position, thus affecting the maximum pump power. Before the sample was extensively bonded, the spurious resonance also affected the break down power, as one can see from the magenta plot in Fig. 6. We therefore conclude that the line homogeneity and the absence of the standing waves are equally important for reaching maximum gain. A perfectly matched line should provide a gain 2–3 dB higher than the one presented in Fig. 4.

### C. Towards perfect impedance matching

To fine tune the impedance to  $50\ \Omega$ , we deposited 200 nm of aluminum oxide on top of the whole chip. To ensure a high quality and continuity of oxide layer, we used atomic layer deposition (ALD) technique (0.85 Å/cycle, thermal oxide at  $300\ ^\circ\text{C}$ , base pressure  $10^{-6}$  mbar). The desired ALD aluminum oxide thickness was estimated by modeling the d.c. electrostatic capacitance per unit length using Comsol. Note that the ALD layer did not significantly affect the impedance of the tapers, because the typical ground-to-strip gap in tapers is much higher than the oxide thickness. As shown in Fig. 7 (bottom red), the deposition of aluminum oxide increased the per unit length capacitance and eliminated the dominant contribution to gain variations in the transmission spectrum as a result of a near perfect match to the  $50\ \Omega$  measurement circuitry. Accordingly, the first and second stopbands in the transmission spectrum were shifted towards lower frequencies and the  $3f$  bandgap became much more pronounced. On the other hand, at frequencies above  $\sim 8$  GHz, the transmission looks more perturbed, which is an expected result of the downscaling of the spurious resonance spectrum. An unexpected feature is spurious resonances at frequencies around  $\sim 2$  GHz, possibly due to increased coupling to some box resonance. Unexpectedly, the ALD deposition resulted in substantial reduction of the maximum pump power the line can

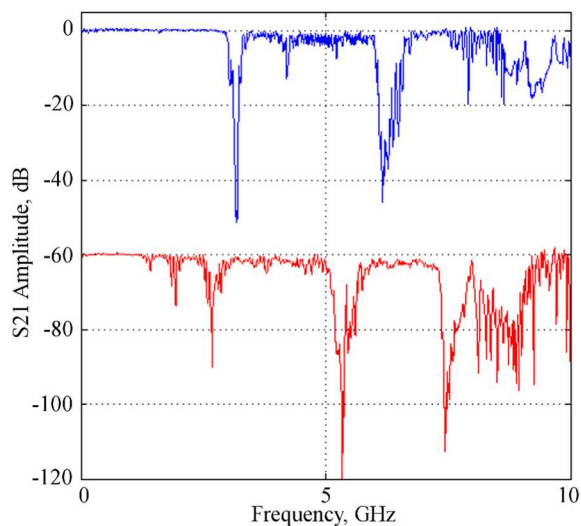


FIG. 7. S21 transmission spectra of combined high/low-KI device, before  $\text{Al}_2\text{O}_3$  deposition (top, in blue) and after (bottom, in red). Red trace is shifted by  $-60$  dB for clarity.

withstand: from  $-14$  dBm to  $-16.5$  dBm. Accordingly, the maximum achievable gain was only 2.7 dB. Likely this was a result of mechanical stress applied to weak spots, but we cannot also exclude that this was a consequence of an enhanced coupling to environmental resonances. However, we shall note that once the kinetic inductance of NbN film is known, the ALD layer is not actually needed: the design could be directly adjusted to  $50\ \Omega$  impedance.

### V. DISCUSSION

To bridge the gap between quantum-limited parametric amplifiers and state of the art semiconductor HEMTs, a gain of about  $\times 40$  is needed. Once the signal is raised  $\sim 16$  dB above the quantum noise level, it can be further boosted with a cascaded HEMT amplifier.

An obvious way to get a higher gain is to make the line longer. This, however, is not a trivial endeavor. The whole fractal structure has  $\sim 2 \times 10^6$  rectangular elements; a failure to develop just one (due to, for example, a dust particle) results in a short and spoils the whole device. For a limited number of shorts, it is possible to eliminate them with FIB etching, for a longer line the FIB technique would be impractical. To maintain the device yield at the acceptable level, a higher class clean room environment is needed.

Another straightforward improvement would be to fabricate the device on a 6 in. wafer. Having in mind the line gain  $\sim 1$  dB  $\text{cm}^{-1}$ , the whole amplifier could then be implemented as a straight line, thus eliminating the residual impedance variations and unfavorable coupling to slot modes. Moreover, a straight fractal structure, just  $\sim 100\ \mu\text{m}$  wide, can be encapsulated in a package free of spurious resonances. Also, for a straight line, the ground plane has the simplest possible geometry, thus reducing the spectral density of ground plane resonances. As our data suggest, once the Fabry-Pérot type oscillations in transmission are eliminated by a proper  $50\ \Omega$  matching, the ripples coming from coupling to spurious resonances present the next substantial design challenge. For all TWAs based on a standard coplanar line, the very long ( $\sim 150\lambda$ ),<sup>17</sup> ( $\sim 423\lambda$ )<sup>18</sup> lines should inevitably couple to many spurious resonances. To be placed on a chip, the  $\sim 1$  m or  $\sim 2$  m line must be somehow folded (as a meander or a spiral), thus imposing non-trivial shape on the ground plane. For such a “patterned” ground plane, the high spectral density of spurious resonances could be on par with Fabry-Pérot spectrum and the destructive effect of these ground plane resonances was recently discussed in literature.<sup>29</sup> In this respect, the fractal design is apparently advantageous because the line is about ten times shorter than in Ref. 17. On the other hand, the fractal line has an increased transversal dimension, which makes it more vulnerable to parasitic resonances. An ultimate remedy would be to implement the same fractal structure with  $0.5\ \mu\text{m}$  design pitch, i.e., to shrink the whole structure by a factor of 2. This will not change the capacitance, but will reduce the parasitic coupling by a factor of 4 (for dipole coupling), so that the residual ripples will be suppressed below the acceptable level. Unfortunately,  $0.5\ \mu\text{m}$  design rule makes the design more vulnerable to dust inclusions and therefore also calls for higher class clean room facilities.

The last but not the least issue we shall discuss is the dispersion engineering. Same as in the original paper by Eom *et al.*,<sup>17</sup> we also found it difficult to arrange a strong enough impedance perturbation to provide sufficient engineered phase shift around the first dispersion band. The reason for this is that the line inductance is a weak function of the line width, so that practically it is not possible to change in, say, twice by varying the line geometry.

Our multilayer design presents a radically different possibility for dispersion engineering by combining central strip sections with and without kinetic inductance. Deploying kinetic inductance as a design parameter, it is possible to arrange 2–3 fold steps in the line impedance; simulations show that the resulting dispersion should be more than adequate.

## VI. CONCLUSION

We have demonstrated that combining the high kinetic inductance of the central strip and quasi-fractal strip-to-ground capacitors one can build a microwave line with the phase velocity as low as  $\sim 3\%$  of the speed of light. Due to enhanced electrical length (for a given physical length), such a line delivers a parametric gain up to  $\sim 0.5$  dB cm<sup>-1</sup>. The presented design allows to cope with two main gain limiting factors: the weak spots in the line and the standing waves due to reflections on the terminals. First, a shorter line is more homogeneous; the break down pump power for the weakest point being just  $\sim 2$  dB below that for the rest of the line. Second, the versatility of the design allows to balance the high kinetic inductance of the central strip with enhanced capacitance of fractal elements in order to keep the line impedance close to 50  $\Omega$  and to suppress the standing waves. Next, we have demonstrated that once the line is properly matched to terminals and the dominant contribution to Fabry-Pérot type ripples on transmission spectrum is eliminated, there are still some stochastic perturbations on the transmission spectrum due to residual coupling to ground plane resonances. We have deployed the multilayer fabrication technology to suppress the kinetic inductance of the ground plane elements in order to up-shift the spectrum of spurious resonances. We have shown that with this technique it is possible to make the transmission spectrum essentially clean and flat up to 8 GHz, moving closer to a practically useful KI-TWPA. Finally, we have argued that a device implemented on a 6 in. wafer with 0.5  $\mu$ m design rule should routinely deliver a parametric gain above 16 dB, which is needed to cascade semiconductor HEMT and quantum-limited parametric amplifiers.

## ACKNOWLEDGMENTS

The devices were fabricated in Chalmers MC2 Nanofabrication Laboratory. We would like to thank V. Shumeiko for fruitful discussions and S. Charlebois for

technical support. We are grateful to Marie Curie Initial Training Action (ITN) Q-NET 264034 and Linne 5920344 for financial support.

- <sup>1</sup>N. Bergeal, F. Schackert, M. Metcalfe, R. Vijay, V. E. Manucharyan, L. Frunzio, D. E. Prober, R. J. Schoelkopf, S. M. Girvin, and M. H. Devoret, *Nat. Lett.* **465**, 64 (2010).
- <sup>2</sup>J. Hansryd, P. A. Andrekson, M. Westlund, J. Li, and P. O. Hedekvist, *IEEE J. Sel. Top. Quantum Electron.* **8**, 506 (2002).
- <sup>3</sup>J. Weber, *Phys. Rev.* **108**, 537 (1957).
- <sup>4</sup>J. P. Gordon and L. D. White, *Proc. IRE* **46**, 1588 (1958).
- <sup>5</sup>W. H. Louisell, A. Yariv, and A. E. Siegman, *Phys. Rev.* **124**, 1646 (1961).
- <sup>6</sup>M. W. Pospieszalski, *IEEE Microwave Mag.* **6**, 62 (2005).
- <sup>7</sup>R. C. Clauss and J. S. Shell, "Ruby Masers," in *Low-Noise Systems in the Deep Space Network, Deep Space Communication and Navigation Series*, edited by M. S. Reid (Jet Propulsion Laboratory, Caltech, 2008).
- <sup>8</sup>M. Oxborrow, J. D. Breeze, and N. M. Alford, *Nature* **488**, 353 (2012).
- <sup>9</sup>Z. Tong, C. Lundström, P. A. Andrekson, M. Karlsson, and A. Bogris, *IEEE J. Sel. Top. Quantum Electron.* **18**, 1016 (2012).
- <sup>10</sup>Z. Tong, C. Lundström, P. A. Andrekson, C. J. McKinstry, M. Karlsson, D. J. Blessing, E. Tipsuwannakul, B. J. Puttnam, H. Toda, and L. Grüner-Nielsen, *Nat. Photonics* **5**, 430 (2011).
- <sup>11</sup>R. Movshovich, B. Yurke, P. G. Kaminsky, A. D. Smith, A. H. Silver, R. W. Simon, and M. V. Schneider, *Phys. Rev. Lett.* **65**, 1419 (1990).
- <sup>12</sup>O. Yaakobi, L. Friedland, C. Macklin, and I. Siddiqi, *Phys. Rev. B* **87**, 144301 (2013).
- <sup>13</sup>J. Y. Mutus, T. C. White, R. Barends, Y. Chen, Z. Chen, B. Chiaro, A. Dunsworth, E. Jeffrey, J. Kelly, A. Megrant, C. Neill, P. J. J. O'Malley, P. Roushan, D. Sank, A. Vainsencher, J. Wenner, K. M. Sundqvist, A. N. Cleland, and J. M. Martinis, *Appl. Phys. Lett.* **104**, 263513 (2014).
- <sup>14</sup>T. C. White, J. Y. Mutus, I. C. Hoi, R. Barends, B. Campbell, Y. Chen, Z. Chen, B. Chiaro, A. Dunsworth, E. Jeffrey, J. Kelly, A. Megrant, C. Neill, P. J. J. O'Malley, P. Roushan, D. Sank, A. Vainsencher, J. Wenner, S. Chaudhuri, J. Gao, and J. M. Martinis, *Appl. Phys. Lett.* **106**, 242601 (2015).
- <sup>15</sup>R. W. Landauer, U.S. patent 3,111,628 (19 November 1963).
- <sup>16</sup>A. L. Cullen, *Nature* **181**, 332 (1958).
- <sup>17</sup>H. B. Eom, P. K. Day, H. G. LeDuc, and J. Zmuidzinas, *Nat. Phys.* **8**, 623 (2012).
- <sup>18</sup>C. Bockstiegel, J. Gao, M. R. Vissers, M. Sandberg, S. Chaudhuri, A. Sanders, L. R. Vale, K. D. Irwin, and D. P. Pappas, *J. Low Temp. Phys.* **176**, 476 (2014).
- <sup>19</sup>R. Klopfenstein, *Proc. IRE* **44**, 31 (1956).
- <sup>20</sup>J. Gao, M. Vissers, M. Sandberg, S. Chaudhuri, C. Bockstiegel, C. Abeles, K. Irwin, and D. Pappas, APS Meet. **59**(1), Q38.00012 (2014); see <http://meetings.aps.org/link/BAPS.2014.MAR.Q38.12>.
- <sup>21</sup>P. K. Day, B. H. Eom, H. G. LeDuc, J. Zmuidzinas, C. Groppi, P. Mauskopf, J. Lamb, and D. Woody, *IEEE Infrared, Millimeter, Terahertz Waves* **39**, 1 (2014).
- <sup>22</sup>A. J. Annunziata, D. F. Santavica, L. Frunzio, G. Catelani, M. J. Rooks, A. Frydman, and D. E. Prober, *Nanotechnology* **21**, 445202 (2010).
- <sup>23</sup>S. E. De Graaf, A. V. Danilov, A. Adamyán, T. Bauch, and S. E. Kubatkin, *J. Appl. Phys.* **112**, 123905 (2012).
- <sup>24</sup>S. Chaudhuri, J. Gao, and K. Irwin, *IEEE Trans. Appl. Supercond.* **25**, 1500705 (2015).
- <sup>25</sup>R. Landauer, *IBM J. Res. Dev.* **4**, 391 (1960).
- <sup>26</sup>A. A. Adamyán, S. E. de Graaf, S. E. Kubatkin, and A. V. Danilov, *Supercond. Sci. Technol.* **28**, 085007 (2015).
- <sup>27</sup>G. Zou, M. Jain, H. Zhou, H. Luo, S. A. Baily, L. Civalo, E. Bauer, T. M. McCleskey, A. K. Burrell, and Q. Jia, *Chem. Commun.* **2008**, 6022.
- <sup>28</sup>K. Ilin, D. Henrich, Y. Luck, Y. Liang, M. Siegel, and D. Y. Vodolazov, *Phys. Rev. B* **89**, 184511 (2014).
- <sup>29</sup>M. R. Vissers, R. P. Erickson, H. S. Ku, L. Vale, X. Wu, G. C. Hilton, and D. P. Pappas, *Appl. Phys. Lett.* **108**, 012601 (2016).